PAPER

DERnet: a deep neural network for end-to-end reconstruction in magnetic particle imaging

IOP Publishing Phys. Med. Biol. 69 (2024) 015002 https://doi.org/10.1088/1361-6560/ad13cf

Physics in Medicine & Biology

IPEM Institute of Physics and Engineering in Medicine

RECEIVED
26 July 2023

REVISED
5 November 2023

ACCEPTED FOR PUBLICATION
8 December 2023

PUBLISHED
22 December 2023

PAPER

DERnet: a deep neural network for end-to-end reconstruction in magnetic particle imaging

Zhengyao Peng[1,2,3,7], **Lin Yin**[1,2,3,7], **Zewen Sun**[1,2,3], **Qian Liang**[1,2,3], **Xiaopeng Ma**[4], **Yu An**[1,3,5,6,*], **Jie Tian**[1,3,5,6,*] and **Yang Du**[1,2,3,*]

[1] CAS Key Laboratory of Molecular Imaging, Institute of Automation, Beijing, People's Republic of China
[2] School of Artificial Intelligence, University of Chinese Academy of Sciences, Beijing, People's Republic of China
[3] Beijing Key Laboratory of Molecular Imaging, Beijing, People's Republic of China
[4] School of Control Science and Engineering, Shandong University, Jinan, Shandon, People's Republic of China
[5] Key Laboratory of Big Data-Based Precision Medicine (Beihang University), Ministry of Industry and Information Technology, People's Republic of China
[6] School of Engineering Medicine, Beihang University, Beijing, People's Republic of China
[7] Authors contributed equally.
[*] Authors to whom any correspondence should be addressed.

E-mail: yuan1989@ buaa.edu.cn, jie.tian@ia.ac.cn and yang.du@ia.ac.cn

Keywords: magnetic particle imaging, end-to-end reconstruction, deep learning, image reconstruction

Abstract

Objective. Magnetic particle imaging (MPI) shows potential for contributing to biomedical research and clinical practice. However, MPI images are effectively affected by noise in the signal as its reconstruction is an ill-posed inverse problem. Thus, effective reconstruction method is required to reduce the impact of the noise while mapping signals to MPI images. Traditional methods rely on the hand-crafted data-consistency (DC) term and regularization term based on spatial priors to achieve noise-reducing and reconstruction. While these methods alleviate the ill-posedness and reduce noise effects, they may be difficult to fully capture spatial features. *Approach*. In this study, we propose a deep neural network for end-to-end reconstruction (DERnet) in MPI that emulates the DC term and regularization term using the feature mapping subnetwork and post-processing subnetwork, respectively, but in a data-driven manner. By doing so, DERnet can better capture signal and spatial features without relying on hand-crafted priors and strategies, thereby effectively reducing noise interference and achieving superior reconstruction quality. *Main results*. Our data-driven method outperforms the state-of-the-art algorithms with an improvement of 0.9–8.8 dB in terms of peak signal-to-noise ratio under various noise levels. The result demonstrates the advantages of our approach in suppressing noise interference. Furthermore, DERnet can be employed for measured data reconstruction with improved fidelity and reduced noise. In conclusion, our proposed method offers performance benefits in reducing noise interference and enhancing reconstruction quality by effectively capturing signal and spatial features. *Significance*. DERnet is a promising candidate method to improve MPI reconstruction performance and facilitate its more in-depth biomedical application.

1. Introduction

Magnetic particle imaging (MPI) (Gleich *et al* 2005) is a powerful tomography technique, and exhibits notable advantages in terms of high imaging sensitivity, excellent penetration depth, high contrast, linear quantification, and great biosafety (Bauer *et al* 2015, Song *et al* 2018, Bulte 2019, Wang *et al* 2020, Li *et al* 2022). The technique has already shown promise for cancer detection (Yu *et al* 2017, Wang *et al* 2022), intracranial hemorrhage detection (Szwargulski *et al* 2020), hyperthermia guidance (Du *et al* 2019), vasculature imaging (Zhou *et al* 2018), and cell tracking (Rivera-Rodriguez *et al* 2021). MPI measures the magnetization response of magnetic nanoparticles (MNPs) to image their spatial distribution, and introduces system matrix (SM) to describe the

mapping relationship between the response and MNP distribution. The pre-acquired SM is commonly employed to reconstruct the distribution images from MPI signals, and these SM-based methods involve solving an ill-posed problem (Kluth 2018, Kluth *et al* 2018). The ill-posedness leads to significant errors in the reconstructed results even with minimal noise, and unfortunately, the MPI signals contain various types of noise (Storath *et al* 2017, Paysen *et al* 2020). Therefore, effective reconstruction method is required to reduce the impact of the noise while transforming the signals into MPI images of the MNP distribution.

1.1. Traditional reconstruction methods

In traditional reconstruction methods, iterative algorithms have shown superior performance compared to direct algorithms. These iterative algorithms execute the regularization term and data-consistency (DC) term iteratively to achieve the reconstruction (Knopp *et al* 2010, Ilbey *et al* 2017, Knopp *et al* 2017, Yin *et al* 2017). The DC term exerts projection from signals to images, and frequency selection is commonly employed to remove the components with high noise level (Knopp *et al* 2010, 2017). Additionally, weighting and other hand-crafted strategies are also applied selectively (Knopp *et al* 2010). For the regularization terms, the hand-crafted spatial priors such as sparsity are utilized to guide the reconstruction. These priors manifest as regularization terms such as L1 norm, L2 norm, total variation (TV) or their combination (Ilbey *et al* 2017, Knopp *et al* 2017, Yin *et al* 2017, Knopp *et al* 2010, 2021, Lieb and Knopp 2021). Hence, the regularization terms can mitigate the ill-posedness based on desired spatial constraints, ultimately optimizing the reconstruction results and minimizing the impact of noise.

As previously mentioned, traditional approaches for MPI reconstruction typically employ the DC term and regularization term, which encompass a variety of widely used methodologies. The most frequent approach is based on the L2-norm and algebraic reconstruction technique (ART), which shows moderate reconstruction efficiency (Knopp *et al* 2010, 2021). However, it exhibits limited noise suppression capability (Storath *et al* 2017, Knopp *et al* 2021). The non-negative fused lasso (NFL) model applies L1 and TV terms and can suppress noise better but has lower reconstruction speed (Storath *et al* 2017). The alternating direction method of multipliers (ADMM) with the L1 and TV terms has the comparable reconstruction quality to NFL and predominant efficiency (Ilbey *et al* 2017). Nevertheless, hand-crafted priors of the above methods may be difficult to fully capture the spatial features of the MNP distribution, limiting their ability to reduce noise influence when data do not fully satisfy the assumed priors (Knopp *et al* 2017, Storath *et al* 2017). In addition, the regularization parameters can exert a significant influence on the result (Ilbey *et al* 2017, Storath *et al* 2017, Kluth *et al* 2018), requiring fine-tuning to preserve details and reduce noise interference.

1.2. Deep learning-based methods

In recent years, data-driven methods have been proposed to mitigate the impact of noise without relying on hand-crafted DC and regularization terms. The deep image prior (DIP) employs the intrinsic ability of the network to regularize ill-posed inverse problems and performs iterations based on the DC during the reconstruction process (Dittmer *et al* 2020, Knopp and Grosser 2022). DIP requires no specific regularization terms or pre-training, but it has poor reconstruction efficiency compared to other methods. PP-MPI applies a trained denoising network as the regularization term and integrates it into the ADMM algorithm. Like DIP, PP-MPI does not require specifying regularization terms and achieves much faster reconstruction speed (Askin *et al* 2022). However, directly adopting an image denoising model as a reconstruction prior may potentially limit its performance, and the iteration number remains undetermined. TheDEQ-MPI (Güngör *et al* 2023) demonstrates improved reconstruction quality and comparable reconstruction speed to $ADMM_{L1}$ by using a novel deep equilibrium reconstruction with learned consistency. Additionally, while direct image reconstruction approaches based on deep learning have demonstrated superiority in reconstructing simulated data (Chae 2017, von Gladiss *et al* 2022), they encounter limitations when it comes to real phantom data. Besides supervised learning algorithms, contrastive learning has also been used in MPI reconstruction (Schrank and Schulz 2023). However, the approach has not yielded satisfactory results yet. Moreover, some reconstruction methods in other medical modalities also have the potential to be applied to MPI reconstruction. MRI reconstruction based on the compressed sensing is also to solve an ill-posed inverse problem (Quan *et al* 2018). Hence, some classical deep learning methods in MRI reconstruction, such as ADMM-Net (Yang *et al* 2018), might be applicable to MPI reconstruction.

1.3. Our method

In this paper, we present a deep neural network called DERnet for end-to-end reconstruction in MPI. Unlike existing DIP and PP-MPI methods, DERnet can directly reconstruct images from signals without iterative processing. The design of DERnet draws inspiration from traditional reconstruction methods, comprising of a feature mapping (FM) subnetwork and a post-processing subnetwork. The FM emulates the DC component of

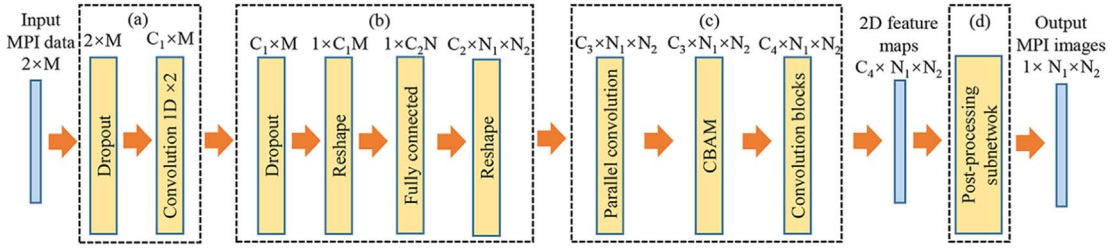

Figure 1. The framework of the DERnet, which is composed of a FM subnetwork and a post-processing subnetwork. The FM subnetwork is divided into (a) signal data processing module, (b) domain transformation module, and (c) feature extraction and attention module. (d) The post-processing subnetwork. The output size of each sub-module is represented as the number of channels × the feature map size of each channel. C_1, C_2, C_3 and C_4 represent the channel number of feature maps. N_1, N_2, N, and M represent the feature map size of each channel. The specific values of these parameters are provided in section 3.3 DERnet implementation.

traditional methods, primarily applied to filtering noise and extracting spatial features from signals. The post-processing subnetwork optimizes reconstruction results based on learned features, resulting in reduced noise output, and from this perspective, it has similar effects to the regularization term. Our proposed method emulates both the DC and regularization terms but is data-driven instead of hand-crafted. Consequently, DERnet can better capture signal and MNP distribution features, thereby achieving superior fidelity and noise suppression. Experiment results demonstrate that our method offers competitive reconstruction efficiency and outperforms the state-of-the-art algorithms with an improvement of 0.9–8.8 dB in terms of peak signal-to-noise ratio (PSNR) under various noise levels. Furthermore, DERnet can be employed for measured data reconstruction with improved fidelity and reduced noise.

2. Methods

The proposed DERnet is data-driven, but there is no ground-truth for the measured MPI signals (Storath *et al* 2017, Knopp *et al* 2010, 2021). Thus, we use simulation data for training and evaluating the method quantitatively. In this section, we first introduce the simulation method that is used to generate the MPI signals. We then elaborate on the network architecture. Finally, we present the training and prediction strategies for DERnet.

2.1. Simulation

It is still an unsolved problem to find a sufficiently accurate model to simulate the behavior of large numbers of MNPs in MPI (Kluth *et al* 2019, Li *et al* 2023). There are notable disparities between the measured and simulated data using the mathematic model alone. Thus, to achieve higher fidelity between simulated and actual data, we simulated the MPI signals with the measured calibration and simulated phantoms. The measured calibration $A_m \in \mathbb{C}^{M\times N}$ is commonly considered as the most accurate SM (Knopp *et al* 2017, 2021) (M is the number of selected frequency components, and N is of the number of the voxels). It is captured using a small MNP sample to traverse on the imaging grids. The MPI signal $\boldsymbol{b}_s \in \mathbb{C}^M$ is simulated as the following:

$$\boldsymbol{b}_s = \boldsymbol{A}_m \boldsymbol{c}_s + \boldsymbol{n}_s, \tag{1}$$

where $\boldsymbol{c}_s \in \mathbb{R}^N$ is the simulated image vector, $\boldsymbol{n}_s \in \mathbb{C}^M$ is the additive noise. Considering that the MPI data measured with different MPI devices and scanning parameters exit disparities, the $\boldsymbol{A}_m$ is not universally applicable.

2.2. DERnet

DERnet is inspired by traditional methods in MPI reconstruction (Knopp *et al* 2010, Ilbey *et al* 2017, Knopp *et al* 2017, Storath *et al* 2017) and consists of two parts: the feature mapping (FM) subnetwork and the post-processing subnetwork. The framework is shown in figures 1 and 2. The FM emulates the DC part of traditional methods and is mainly applied to signal data denoising and mapping signals to spatial features. The post-processing subnetwork is used to extract spatial features and perform optimization of reconstruction results based on learned features.

In DERnet, all convolution layers are equipped with 3×3 convolution kernel (unless otherwise specified), and the weights of neural network layers (e.g. convolution layers, fully connected layers) are initialized using default method in PyTorch. The model does not use predefined/custom filters, and all weights are obtained through end-to-end training in this work. In addition, the number of weights can be calculated using the

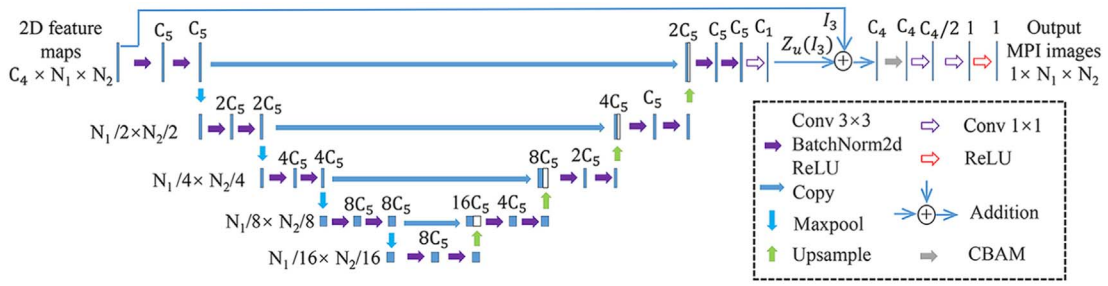

Figure 2. The post-processing subnetwork, which employs a modified Unet. The output of the subnetwork is the reconstruction result of the DERnet. The output size of each sub-module can be represented as the number of channels × the feature map size of each channel. C_4 and C_5 are the channel number of feature maps. N_1, N_2 represent the feature map size of each channel. The specific values of these parameters are provided in section 3.3 DERnet implementation. I_3 is output of the FM subnetwork.

provided input and output information of the sub-modules. Hyperparameters (e.g. C_1-C_5, ρ_0 and ρ_1) are optimized on the validation set, and their specific values can be found in section 3.3. In the following sections, we will provide a detailed description of each submodule in the FM subnetwork and the post-processing subnetwork.

(a) Signal data processing module. In the DC of the traditional method, frequency selection schemes are used to remove the data with low signal-noise ratio (SNR). For FM, the input is also the selected signals (frequency domain), where the two channels represent the real and imaginary components. Furthermore, input data are processed to exert signal denoising through 1D convolution layers ($Z_{1D,1}(\cdot)$, $Z_{1D,2}(\cdot)$) that are equipped with a dropout layer $D(\cdot)$. The output $U_0 \in \mathbb{R}^{C_1\times M}$ of the convolution layers can be described as follows:

$$\boldsymbol{U}_0 = Z_{1D,2}(Z_{1D,1}(D(\boldsymbol{U}_{in},\ \rho_0))), \tag{2}$$

where $\boldsymbol{U}_{in} \in \mathbb{R}^{2\times M}$ is the MPI frequency-domain signal, and ρ_0 is the dropout rate.

(b) Domain transformation module. The DC term is employed to describe the relationship between the signal and spatial distribution of MNPs, and it completes the domain transformation from signal to image. Thus, we design the module in FM to achieve this transformation. Based on the linear model (1), the image vector $\boldsymbol{c}_{\text{rec}} \in \mathbb{R}^N$ can be directly obtained through inverse operations when the noise is neglected. From this observation, the transformation from signal to image can be directly achieved as following:

$$\boldsymbol{c}_{\text{rec}} = \boldsymbol{A}_m^{\dagger}\boldsymbol{b}, \tag{3}$$

where $\boldsymbol{A}_m^{\dagger} \in \mathbb{C}^{N\times M}$ is the pseudo-inverse of $\boldsymbol{A}_m$. This approach is called pseudo-inverse method (Coene *et al* 2013, Baksalary and Trenkler 2021) and it directly transforms the 1D signal data into the 2D spatial data. The output data are vectorized over the rows, and it can be reshaped into two-dimensional images of size N1 × N2.

Inspired by (3), we adopt the fully connection (FC) layer to achieve the domain transformation as following:

$$\boldsymbol{I}_0 = \boldsymbol{W}_{\text{FC}} D(\boldsymbol{U}_0,\ \rho_1) \tag{4}$$

where $\boldsymbol{I}_0 \in \mathbb{R}^{C_2 N}$ is the image vector, $\boldsymbol{W}_{FC} \in \mathbb{R}^{C_2 N\times C_1 M}$ denotes the learned weights in the FC, C_2 and C_1 are the channel number of the feature maps, and ρ_1 is the dropout rate. Compared (3) and (4), similar procedures are performed, and they all obtain the voxel value by weighted sum of frequency-domain signal data. Thus, (5) is adopted for the domain transformation, and the output is defined as $\boldsymbol{I}_1 \in \mathbb{R}^{C_2\times N_1\times N_2}$, where $N = N_1N_2$:

$$\boldsymbol{I}_1 = Z_{\text{reshpe}}(\boldsymbol{I}_0) = Z_{\text{reshpe}}(\boldsymbol{W}_{\text{FC}} D(\boldsymbol{U}_0,\ \rho_1)) \tag{5}$$

where $Z_{\text{reshpe}}(\cdot)$ denotes the reshaping operation.

(c) Feature extraction and attention module. This module is designed to capture abundant semantic information and effectively weight features to highlight important features while reducing noise interference. To extract multi-scale spatial features, we use a parallel convolution block with kernels of 1×1, 3×3, and 5×5. Then, the features are concatenated and fused. The output of the block is defined as $\boldsymbol{I}_2 \in \mathbb{R}^{C_3\times N_1\times N_2}$, where C_3 is the channel number of the feature maps.

$$\boldsymbol{I}_2 = Z_{2D,4}(Z_{\text{cat}}(\boldsymbol{I}_1,\ Z_{2D,1}(\boldsymbol{I}_1),\ Z_{2D,2}(\boldsymbol{I}_1),\ Z_{2D,3}(\boldsymbol{I}_1))), \tag{6}$$

where $Z_{2D,1}(\cdot)$, $Z_{2D,2}(\cdot)$, $Z_{2D,3}(\cdot)$ and $Z_{2D,4}(\cdot)$ denote convolution layers with kernels of 1×1, 3×3, 5×5 and 3×3; Z_{cat} represents concatenation along the channel dimension.

Subsequently, the convolutional block attention module (CBAM) (Woo *et al* 2018) is added to adaptively learn the weights for each feature channel and position based on their importance. Then, a convolution block is adopted for feature fusion, and the output $\boldsymbol{I}_3 \in \mathbb{R}^{C_4 \times N_1 \times N_2}$ can be written as:

$$\boldsymbol{I}_3 = Z_{2D,5}(Z_{\mathrm{CBAM}}(\boldsymbol{I}_2)), \tag{7}$$

where Z_{CBAM} denotes the CBAM, and $Z_{2D,5}$ represents a cascaded convolutional module. $Z_{2D,1}(\cdot)$, $Z_{2D,2}(\cdot)$, $Z_{2D,3}(\cdot)$ and $Z_{2D,5}(\cdot)$ are equipped with batch normalization (BN) and rectified linear activation function (ReLU).

(d) Post-processing subnetwork. In traditional methods, regularization terms are used to add constraints to the reconstructed images based on the desired spatial attributes (e.g. smoothness, sparsity), thereby optimizing the results. DERnet also adopts a subnetwork to post-process reconstruction results based on learned spatial attributes. Incorporating these learned features as constraints contributes to mitigating the ill-posed nature of the reconstruction problem, and hence, it reduces the noise impact on the reconstruction results. In DERnet, a modified Unet is adopted as the post-processing subnetwork. Unet is a classical image segmentation and processing network (Ronneberger and Brox 2015), which is slightly modified in this study. The residual connection is added, and convolution blocks are equipped with ReLU and BN. To output reconstruction images, the channel number of the feature map is reduced to the single and ReLU performs the non-negativity constraint as the final layer. The final output can be described as:

$$\boldsymbol{I}_{\mathrm{output}} = Z_{2D,6}(\boldsymbol{I}_3 + Z_u(\boldsymbol{I}_3)) \tag{8}$$

where $\boldsymbol{I}_{\mathrm{output}} \in \mathbb{R}^{N_1 \times N_2}$ represents the output of DERnet, Z_u denotes the U-shape subnetwork as shown in figure 2, and $Z_{2D,6}$ comprises the operations of single CBAM block, two convolutional layers and single ReLU layer.

2.3. Training and prediction strategies

The normalization $N(\cdot)$ can improve model convergence speed and robustness, and it is written as:

$$N(\boldsymbol{b}) = \boldsymbol{b}/b_{\max}, \tag{9}$$

where $\boldsymbol{b} \in \mathbb{C}^M$ is the frequency-domain signal, and $b_{\max}$ represents the maximum amplitude value of $\boldsymbol{b}$. The prediction result $\boldsymbol{I}_{pd} \in \mathbb{R}^{N_1 \times N_2}$ is followed:

$$\boldsymbol{I}_{pd} = b_{\max} Net_{DER}(N(\boldsymbol{b})) \tag{10}$$

where Net_{DER} denotes DERnet. The $b_{\max}$ is used to weight the reconstruction result, and it is applicable to the case of a linear model as (1) in the absence of excessively strong noise.

The loss function (*Loss*) is the mean square error (MSE) of the prediction results and ground truth as follows:

$$\mathrm{MSE}(\boldsymbol{I}_{pd}, \boldsymbol{I}_{gt}) = \frac{1}{N_1 N_2} \sum_{i=1}^{N_1} \sum_{j=1}^{N_2} [\boldsymbol{I}_{pd}(i, j) - \boldsymbol{I}_{gt}(i, j)]^2, \tag{11}$$

where $\boldsymbol{I}_{gt} \in \mathbb{R}^{N_1 \times N_2}$ denotes the ground truth.

3. Experiment

3.1. Dataset

In this work, the dataset can be divided into simulated and measured data. The simulated data are obtained by assuming the MNP distribution and simulating according to the method in the section 2.1. Hence, the ground truth of the simulated data is the assumed MNP distribution maps. The measured data are got from the MPI device. The ground truth of measured data cannot be obtained. Phantom images or slices in the 3D printer models are provided as reference images to facilitate qualitative comparison.

(a) Simulation dataset. In this paper, 60 000 images from Mixed National Institute of Standards and Technology database (MNIST) (LeCun *et al* 1998) were selected, and processed. The images were cropped, retaining only the central 15 × 15 patch, and then randomly rotated and placed within a random region of the image. Subsequently, they were resized to the specified dimensions, consistent with the grid size of the system matrix. Using these images as simulated phantom, the simulation was performed based on (1) and the Gaussian noise (Storath *et al* 2017, Paysen *et al* 2020) was added. The training dataset consisted of 48 000 data samples at SNRs ranging from 20 to 40 dB. The validation dataset comprised 6000 data samples at SNRs ranging from 20 to 40 dB, and it is adopted to select the used model and the optimal hyperparameters. During the training process, the model that performed best on the validation set is chosen as the final saved

model. The test dataset contained 6000 data samples at a fixed SNR of 30 dB. The procedure outlined in (a) was applied to the data from (b) as well as from (c) and that for both a DERnet was trained.

(b) OpenMPI dataset (Knopp *et al* 2020). OpenMPI is an open-source MPI dataset. For this study, we used the 2D SM calibration data from OpenMPI (experiment number: 2) along with 2D phantom measurement data. The used calibration and phantom data were obtained on a preclinical FFP scanner (Bruker, Ettlingen) with Perimag MNPs (Micromod GmbH, Germany). The 2D SM was measured with the drive-field amplitude of 12 mT × 12 mT × 0 mT, but with 19 × 19 × 19 grid positions. This calibration method can suppress signal interference from out-of-plane MNPs, making the 3D object more accurate after splicing 2D images along the z-axis (Mason *et al* 2022). However, many works for 2D MPI reconstruction only need system matrix with 2D shape (Storath *et al* 2017, Knopp *et al* 2010, 2021). Our work only reconstructed 2D results, and hence, we only extracted the tenth slice of the 2D SM data and only kept the SM rows with SNR $>$ 1.5 dB. The measurements included three 2D phantom data named Shape, Resolution and Concentration. More details can be found in Knopp *et al* (2020).

(c) In-house dataset (Shi *et al* 2023). We evaluated our method on an in-house FFP scanner. The selection gradient was set to [1.7, 1.7] along the X and Y axes, and the driving frequency was 25 kHz. A field of view was set to 22 mm × 22 mm, and a delta sample (2 mm × 2 mm), filled with Perimag MNPs (8.5 mg ml^{-1}), was utilized to acquire the SM with grid 11 × 11. The paralleled cylindrical tube and C-shape phantoms were used for demonstration, and they were filled with Perimag MNPs (8.5 mg ml^{-1}). We preserved the first to thirteenth harmonic for reconstruction.

3.2. Competing methods

(a) ART. ART is a classical reconstruction method for MPI, and Kaczmarz/Tikhonov algorithm was implemented in this paper (Knopp *et al* 2010, 2021). The number of iterations was 10, ensuring convergence, and optimal parameters can be seen in table 1.

(b) ADMM. We implemented ADMM algorithm with three regularization terms: L1, TV and L1+TV (Ilbey *et al* 2017, Askin *et al* 2022). The parameter μ was optimized through experimentation and the number of iterations was 200. For the ADMM$_{\mathrm{L1+TV}}$, $\alpha_{\mathrm{TV}} + \alpha_{\mathrm{L1}} = 1$ and the optimal α_{TV} was also chosen through experimentation. ε was adjusted with SNRs, and it adopted the Euclidean distance of the noise (Ilbey *et al* 2017, Askin *et al* 2022). The optimal parameters were displayed in the table 1.

(c) PP-MPI. The PP-MPI is deep-learning-based method, and it used a trained denoiser as the regularization terms (Askin *et al* 2022). For the training of the denoiser, LR was 0.01, and the standard deviation of the noise was 0.001. and 4000 iterations with ADAM optimizer were employed. For the reconstruction, the optimal parameter could be seen in the in the table 1.

(d) DIP. The DIP used an untrained network whose weights are not determined based on the training dataset, but during the reconstruction (Dittmer *et al* 2020, Knopp and Grosser 2022). In DIP, 0.001 learning rate (LR) and 4000 iterations with ADAM optimizer were employed.

(e) ADMM-Net. The ADMM-Net is deep learning approach, and is a classical unrolling method. The Generic-ADMM-Net (Yang *et al* 2018) was adopted in this work and the optimal parameters were shown in the table 1. LR was 0.01, and 4 iterations with ADAM optimizer were employed.

3.3. DERnet implementation

For the OpenMPI and in-house data, we trained the DERnet separately because of the different SMs. By comparing the performance models trained with different hyperparameter values on the validation set, the optimal hyperparameters are selected. Common set of parameters included $C_1 = 8$, $C_2 = 4$, $C_3 = 16$, $C_4 = 8$, $C_5 = 128$, $\rho_0 = \rho_1 = 0.05$, LR $= 0.001$. According to calibration data, $M = 839$, $N_1 = N_2 = 19$ for OpenMPI data, and $M = 139$, $N_1 = N_2 = 11$ for in-house data. Due to the limitations of the feature map size, only three pooling operations were implemented in post-processing subnetwork during in-house data reconstruction. The DERnet training was implemented in PyTorch on a NVIDIA GeForce RTX 3090 GPU.

3.4. Quantitative assessments

The ground truth of measured data including OpenMPI and in-house data was not available, and their reconstruction results were only assessed visually. Thus, the quantitative assessments were implemented using simulated data obtained via OpenMPI SM. The normalized root MSE (NRSME) was adopted to reflect the data

Table 1. Parameter settings in the competing methods. The simulated data refer to the data with the procedure according to 3.1(a), and the data are obtained using the system matrix from OpenMPI. OpenMPI and inhouse data are got from phantom experiments, and more details can be found in 3.1(b) and 3.1(c).

Dataset	ART (α, iterations)	ADMM_{L1} (μ, iterations)	ADMM_{TV} (μ, iterations)	$\text{ADMM}_{\text{L1+TV}}$ (μ, α_{TV}, iterations)	PP-MPI (iterations)	ADMM-Net (LR, iterations)	DIP (LR, iterations)
Simulated data (20 dB)	0.1, 10	1, 200	10, 200	1, 0.7, 200	10	0.001, 4	0.001, 4000
Simulated data (25 dB)	0.01, 10	1, 200	10, 200	1, 0.8, 200	10	0.001, 4	0.001, 4000
Simulated data (30 dB)	0.01, 10	10, 200	10, 200	10, 0.8, 200	20	0.001, 4	0.001, 4000
Simulated data (35 dB)	0.01, 10	10, 200	100, 200	10, 0.8, 200	30	0.001, 4	0.001, 4000
OpenMPI data	0.01, 10	10000, 200	10000, 200	100, 0.5, 200	50	0.001, 4	0.001, 4000
In-house data	0.001, 10	10, 200	100, 200	10, 0.6, 200	70	0.001, 4	0.001, 4000

fidelity:

$$\mathrm{NRMSE}(\mathbf{I}_{\mathrm{pd}}, \mathbf{I}_{gt}) = \frac{\| \mathbf{I}_{\mathrm{pd}} - \mathbf{I}_{gt} \|_{\mathrm{F}}}{\| \mathbf{I}_{gt} \|_{\mathrm{F}}}, \tag{12}$$

where $\|\cdot\|_{\mathrm{F}}$ donated the Frobenius norm. The peak SNR (PSNR) calculated the ratio between the maximum possible signal power and the power of the error in the images, which caused by the signal noise in this reconstruction task. Thus, it was employed to indicate the impact of signal noise on the quality of reconstruction:

$$\mathrm{PSNR}(\mathbf{I}_{\mathrm{pd}}, \mathbf{I}_{gt}) = 10 \log_{10} \frac{\mathbf{I}^2_{\mathrm{gt,max}}}{\mathrm{MSE}(\mathbf{I}_{\mathrm{pd}}, \mathbf{I}_{gt})}, \tag{13}$$

where $\mathbf{I}_{\mathrm{gt,max}}$ donated the maximum value in $\mathbf{I}_{\mathrm{gt}}$. Structural similarity index measure (SSIM) is a metric based on the perceive visual quality, and can better reflect human evaluation of reconstruction quality:

$$\mathrm{SSIM}(\mathbf{I}_{\mathrm{pd}}, \mathbf{I}_{gt}) = \frac{(2\mu_{pd}\mu_{gt} + c_1)(2\sigma_{pd,gt} + c_2)}{(\mu^2_{pd} + \mu^2_{gt} + c_1)(\sigma^2_{pd} + \sigma^2_{gt} + c_2)}, \tag{14}$$

where μ_{pd}, μ_{gt} are the means of the reconstruction result and ground truth; c_1, c_2 are constants that prevent division by zero; σ^2_{pd}, σ^2_{gt} represent the variances and $\sigma_{pd,gt}$ is the covariance between the reconstruction result and ground truth. All the metrics were directly adopted the functions from skimage (Van der Walt *et al* 2014).

4. Results

4.1. Analyzes on simulated dataset

We first evaluated performance of the DERnet on the simulation dataset against some traditional reconstruction method (ART, $\mathrm{ADMM_{L1}}$, $\mathrm{ADMM_{TV}}$, and $\mathrm{ADMM_{L1+TV}}$), as well as state-of-art deep learning methods (DIP, ADMM-Net and PP-MPI). We performed quantitative assessments with 6000 simulation data obtained via OpenMPI SM, and presented the results in table 2. Among traditional reconstruction methods, $\mathrm{ADMM_{L1+TV}}$ achieves the best quantitative performance. In comparison to it, DERnet can lead to the reduction of 0.067 in NRMSE (31.5%), an enhancement of the 0.032 in SSIM (3.36%) and a 3.2 dB increase in PSNR (12.5%). Among all competing methods except for DERnet, PP-MPI achieves the best performance and significantly outperformed the other competing methods. Compared to PP-MPI, the proposed DERnet can reduce the 0.031 in term of NRMSE (17.5%), improve 0.013 regarding SSIM (1.34%), and increase 1.6 dB in terms of PSNR (5.86%).

Some representative reconstruction results are shown in figure 3. ART yields artifacts and noise in the region without MNPs, but it has a better visual impression than ADMM-based methods. Compared with ART, $\mathrm{ADMM_{L1+TV}}$ achieves a better quantitative performance (table 2), but poorer qualitative results. The difference in regularization terms may lead to this contradiction. $\mathrm{ADMM_{L1+TV}}$ uses the L1 norm and TV term, which make the reconstructed images sparser (pixel values tend to be 0) than that of the ART with L2 norm. Hence, $\mathrm{ADMM_{L1+TV}}$ offers less noise and has better quantitative performance. However, the TV term also results in staircasing effects (Wang *et al* 2018, Knopp *et al* 2017, Storath *et al* 2017), and the reconstruction results are separated into flat regions by artifact boundaries. Hence, the results of the $\mathrm{ADMM_{L1+TV}}$ have a worse visual impression than ART. Moreover, $\mathrm{ADMM_{L1}}$ yields obvious noise, and $\mathrm{ADMM_{TV}}$ offers less noise but exhibits staircasing effects. The results of the traditional methods demonstrate that traditional reconstruction methods can partially suppress noise, but suffer from inadequate noise reduction or staircasing effects due to the limitation of hand-crafted DC and prior terms. DIP suffers most severely from noise, and the randomness in DIP algorithm may lead to some poor results. The ADMM-Net demonstrates satisfactory noise-suppression capabilities in the region without MNPs, but tends to blurry the images. PP-MPI and proposed DERnet outperform the others. Furthermore, DERnet is significantly better than PP-MPI from the error maps. Overall, the proposed DERnet demonstrates significant superiority over other approaches based on quantitative and qualitative analysis.

4.2. Denoising experimental results

We performed denoising experiment with 50 simulated phantoms. The ideal simulation data were exposed with the noise at the different SNRs, including 20 dB, 25 dB, 30 dB and 35 dB. All data are processed according to 3.1. (a) with the system matrix from OpenMPI. The quantitative assessments are displayed in table 3. As expected, the performance of various methods exhibits an overall declining trend with the increase of noise intensity. The robustness of the $\mathrm{ADMM_{L1}}$ is relatively poor. The reconstruction results of ADMM-Net are almost unchanged under different noise interference, which is consistent with the conclusion in (Yang *et al* 2018). Except for

Table 2. Comparison based on simulated data at a fixed SNR of 30 dB (mean ± std), the simulated data are obtained according to 3.1(a) using the system matrix from OpenMPI.

Metrics	ART	$ADMM_{L1}$	$ADMM_{TV}$	$ADMM_{L1+TV}$	PP-MPI	DIP	ADMM-Net	DERnet
NRMSE	0.221 ± 0.0699	0.297 ± 0.108	0.269 ± 0.105	0.213 ± 0.0836	0.177 ± 0.0711	0.444 ± 0.252	0.466 ± 0.109	$\mathbf{0.146 \pm 0.0548}$
SSIM	0.834 ± 0.0916	0.911 ± 0.0588	0.906 ± 0.0621	0.952 ± 0.0395	0.971 ± 0.0211	0.803 ± 0.180	0.776 ± 0.087	$\mathbf{0.984 \pm 0.0114}$
PSNR	25.2 ± 3.22	22.8 ± 3.28	23.8 ± 2.90	25.7 ± 3.04	27.3 ± 3.15	20.0 ± 4.94	18.6 ± 2.53	$\mathbf{28.9 \pm 3.31}$

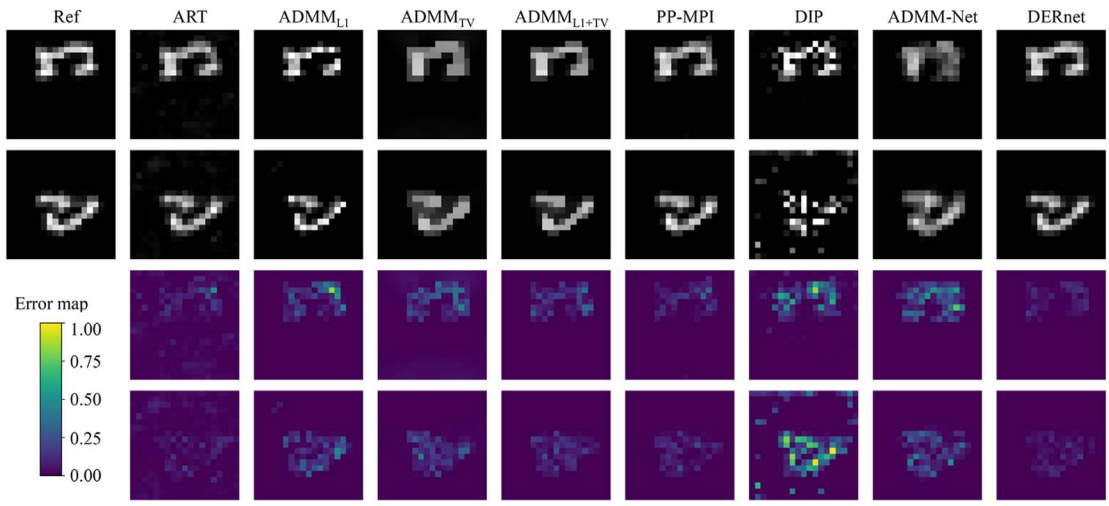

Figure 3. Representative reconstruction results and error maps based on the simulated test dataset with the SNR of 30 dB. The test data are obtained according to 3.1(a) using the system matrix from OpenMPI.

Table 3. Comparison based on simulated data at SNRs ranging from 20 to 35 dB. The PSNR is reported as mean ± std, and the simulated data are obtained according to 3.1(a) using the system matrix from OpenMPI.

Dataset	ART	ADMM$_{L1}$	ADMM$_{TV}$	ADMM$_{L1+TV}$	PP-MPI	DIP	ADMM-Net	DERnet
20 dB	21.2 ± 2.23	17.6 ± 1.93	20.2 ± 2.35	21.3 ± 2.39	23.0 ±2.34	17.4 ± 3.35	18.3 ±1.87	**24.0 ± 2.82**
25 dB	23.2 ± 2.20	21.6 ± 2.51	24.1 ± 2.71	25.6 ± 2.19	25.7 ± 2.60	18.9 ± 4.21	18.4 ±1.84	**26.6 ± 2.73**
30 dB	24.9 ± 2.57	22.9 ± 2.57	24.0 ± 2.61	25.8 ± 2.48	27.3 ± 2.48	19.2 ± 5.47	18.4 ± 1.86	**28.4 ± 2.82**
35 dB	25.7 ± 2.93	26.0 ± 2.96	26.9 ± 3.10	28.5 ± 2.94	29.0 ± 2.91	20.7 ± 4.01	18.4 ± 1.88	**29.6 ± 3.27**

ADMM-Net, DIP exhibits minimal reduction in terms of PSNR, but the overall performance of ADMM-Net and DIP is unsatisfactory. The proposed DERnet outperforms other methods, and the PSNR declines 5.6 dB as the SNR of the signals decreases from 35 dB to 20 dB. Although the PSNRs of ART, DIP and ADMM-Net results decrease less, their PSNRs are lower by 2.8–11.2 dB compared with our method. Under various noise levels, the proposed DERnet outperforms those state-of-the-art algorithms with an average improvement of 0.9–8.8 dB in terms of PSNR. Some representative reconstruction results are displayed in figure 4. Similar to the quantitative analysis, the proposed DERnet achieves superior fidelity and demonstrates better denoising ability. It is worth noting the parameters of most other methods are optimized at different SNRs, while DERnet remains unchanged. Overall, the denoising experimental results demonstrate the advantages of our approach in suppressing noise interference.

4.3. OpenMPI data reconstruction results

In this study, we evaluated the reconstruction performance of the proposed method using the 2D phantom measurement from OpenMPI. The DERnet was trained with the simulation data, and used to reconstruct the measured data. The data consisted of some slices of the three phantom measurement data mentioned above, and the normalized reconstruction images using their maximum values are shown in figure 5. It was worth mentioning that the ground truth was not available, and the reference images were from the computer-aided design model of the phantoms. Thus, we could only perform qualitative analysis based on visual observations.

For the resolution phantom, the reconstruction results of the ART and DIP show noticeable noise in the surroundings. ADMM$_{L1}$ exhibits information loss in its results, and ADMM$_{TV}$ and ADMM$_{L1+TV}$ suffer from blurred artifacts. The ADMM-Net yields poorest reconstruction results, which is consistent with the analysis results on the simulation dataset. More modifications based on MPI principles and characteristics may improve the performance of ADMM-Net. The PP-MPI and DERnet have the similar reconstruction quality and outperform the others. For the Concentration phantom, all the method can reconstruct the region with the minimum concentration MNPs, but it is visually inconspicuous in the results of the ADMM$_{TV}$ and ADMM$_{L1+TV}$. Moreover, there is some noise in the results of ART, DIP, ADMM$_{L1}$ and PP-MPI, and the ADMM-Net fails to reconstruct the distribution of magnetic particles well. Compared with the other methods, the DERnet shows better noise suppression and information preservation capabilities.

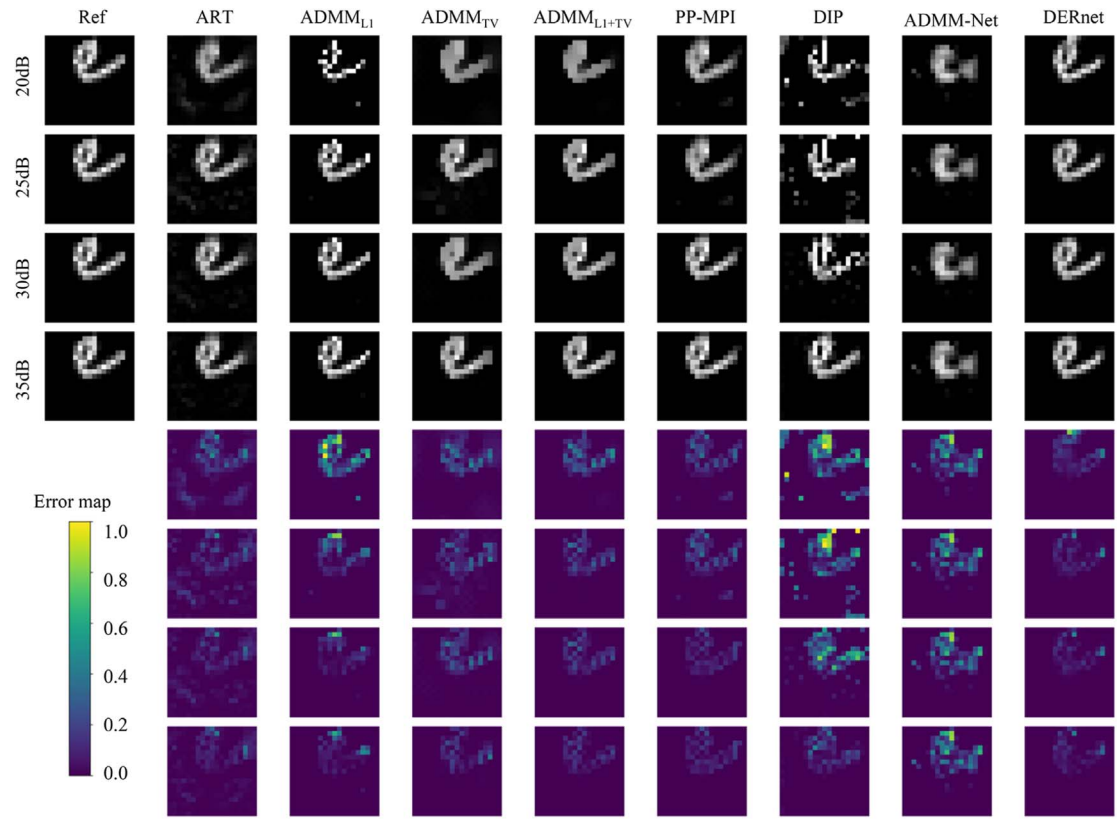

Figure 4. Representative results in the denoising experiment and error maps using the indicated methods, and the test data are obtained according to 3.1(a) using the system matrix from OpenMPI. The SNRs of the data are 20–35 dB.

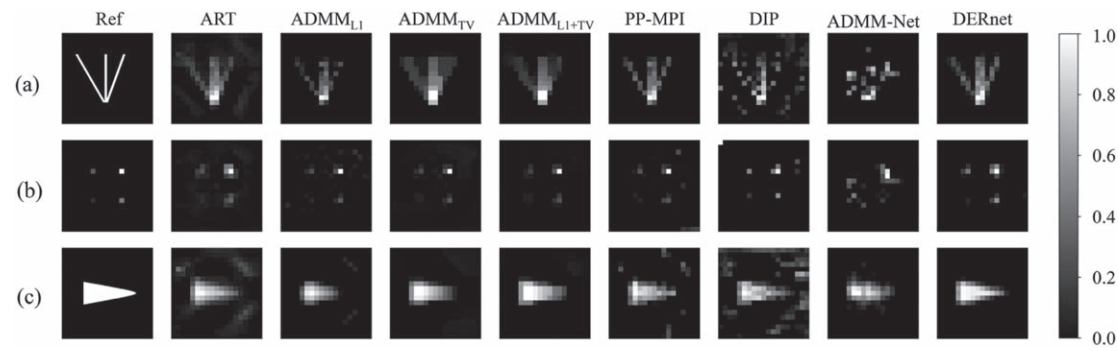

Figure 5. Reconstruction results of OpenMPI phantom data using the indicated methods. Reconstructions are shown for the (a) 11th slice of the Resolution phantom data in the OpenMPI database, (b) 7th slice of the Concentration phantom data and (c) 10th slice of the Shape phantom data.

For the shape phantom, ADMM$_{L1}$ and ADMM-Net exhibit information loss, and the results of the ADMM$_{TV}$ and ADMM$_{L1+TV}$ are blurred. The ART, DIP and PP-MPI did not effectively suppress noise. As expected, the proposed method shows the best performance among all competing methods.

The parameters of the competing methods are selected based on visual optimization, and the proposed network is not fine-tuned after training. Thus, it can be seen that our method can robustly reconstruct the measured data with the unknown noise and achieve the best reconstruction performance compared to other reconstruction methods.

4.4. In-house data reconstruction results

In this study, we demonstrated the reconstruction performance of our method on an in-house dataset. Due to the different SM used in the reconstruction tasks, we retrained the network. The normalized reconstruction results are shown in figure 6 along with the corresponding reference images.

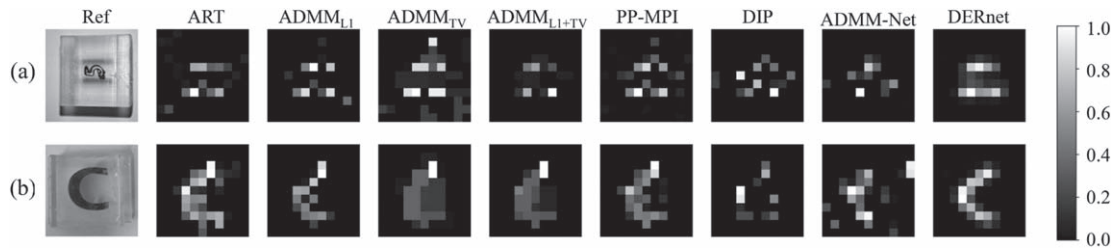

Figure 6. Reconstruction results of in-house data using the competing methods and DERnet. (a) The reference image and reconstructions of cylindrical phantom data (two parallel cylindrical tubes with 5 mm distance). (b) The reference image and reconstructions of C-shape phantom data.

Table 4. The number of iterations and mean reconstruction time, and data are simulated according to 3.1(a) using the system matrix from OpenMPI.

	ART	ADMM$_{L1}$	ADMM$_{TV}$	ADMM$_{L1+TV}$	PP-MPI	DIP	ADMM-Net	DERnet
Iteration numbers	10	200	200	200	20	4000	4	
Time (s)	4.84	0.113	0.882	0.904	0.120	95.5	0.0439	**0.0380**

For the cylindrical phantom, DIP and ADMM-Net fail to reconstruct the distribution of magnetic particles well. The ART, ADMM$_{L1}$, ADMM$_{TV}$ and PP-MPI produce residual noise outside of the two cylinders, and ADMM$_{L1+TV}$ shows the information loss. Our DERnet presents less noise outside of the two cylinders and some low-intensity artifacts. Overall, our method still maintained superior or comparable reconstruction quality compared to other methods.

For the C-shape phantom, ADMM-Net, ART and DIP yields residual noise and fails to reconstruct a complete phantom shape. Distorted information is presented in the upper half of ADMM$_{L1}$ reconstruction result, and the concentration in certain regions of ADMM$_{TV}$ and ADMM$_{L1+TV}$ results exhibits significantly higher intensity, which deviates noticeably from reality. In comparison, the trained DERnet reconstructs the C-shaped phantom with less noise and higher fidelity.

The parameters for the alternative algorithms are selected based on their visually optimal performance. In comparison, the trained DERnet does not require fine-tuning and exhibits significant superiority over other approaches in terms of reconstruction quality.

4.5. Reconstruction time

Table 4 lists the mean reconstruction time of 50 simulated data with a SNR of 30. All methods were implemented in Python and deployed on a NVIDIA GeForce RTX 1080 GPU without any explicit parallelization. The DIP uses an untrained network, which requires a particularly large number of iterations to update model parameters until satisfactory results are obtained. The ART is also relatively inefficient, and the ADMM-based and PP-MPI can complete the inference in less time. The ADMM-Net requires matrix inversion, which limits the reconstruction speed. Moreover, Though PP-MPI model is more lightweight, it requires multiple iterations, which reduces its reconstruction efficiency. DERnet can complete the end-to-end reconstruction of the MPI images without iterations, and hence, it offers the highest reconstruction efficiency among all the methods.

5. Discussion

MPI images is effectively affected by signal noise as its reconstruction is an ill-posed inverse problem. To improve the MPI reconstruction quality and reduce the noise interference, we proposed an end-to-end reconstruction network called DERnet. Different from the traditional methods, the DERnet seeks to map the MPI signals to the MNP distribution in a data-driven manner, and it emulates the regularization term and DC using an FM subnetwork and a post-processing subnetwork, respectively, but is learning-based. The FM is applied to preliminary filtering of signal noise and extracting spatial features from signals. The post-processing subnetwork optimizes reconstruction results based on learned spatial features, resulting in reduced noise output. By doing so, DERnet can better capture signal and spatial features without relying on hand-crafted priors and strategies, thereby effectively reducing noise interference and achieving improved fidelity.

Quantitative assessments show that our proposed method yielded less noise in reconstruction results and offered robust performance for various data types and noise levels. Compared with the competing algorithms, the DERnet outperforms the state-of-the-art algorithms 0.9–8.8 dB in PSNR across the simulated data with various SNRs ranging from 20 to 35 dB. Furthermore, the model trained on the simulated data can be employed to measured MPI data, whose noise distribution is unknown. The reconstruction results of the openMPI and in-house data show that our method achieve the superior quality with improved fidelity and reduced noise. Moreover, Due to its enhanced feature extraction capability, our method successfully suppresses the noise effects on the reconstruction results without requiring parameter adjustments based on the noise levels. Additionally, our end-to-end method does not require the iterations, which is beneficial to the reconstruction efficiency.

It is observed that DIP shows relatively limited performance in this paper, and one possible reason is that its update only relies on the DC term (Dittmer *et al* 2020, Askin *et al* 2022). It might lead to a high sensitivity to noise and a less accurate reconstruction result, especially when dealing with complex imaging tasks or datasets with high noise levels. Additionally, DIP's weight optimization may be computationally expensive and time-consuming, making it difficult to apply in real-time applications. Overall, while DIP shows promise for the MPI reconstruction, further research is needed to optimize its performance and address its limitations.

ADMM-Net is an unrolling-based network, which was first used for compressive sensing MRI (Yang *et al* 2018). In this work, the ADMM-Net framework is directly used as a competing algorithm, and some implementation details have been modified. Overall, the ADMM-Net demonstrates extremely strong noise robustness as shown in table 3. Nonetheless, the reconstructed results were of relatively poor quality. The results might be limited by the model's design, which comprises just a few convolutional and nonlinear layers. However, increasing the number of model layers or iterations could easily lead to the model converging to the extremum, and outputting all-zero images. More modifications based on MPI principles and characteristics may improve the performance of ADMM-Net. Additionally, matrix inversion is time-consuming, which limits the reconstruction speed of ADMM-Net.

In this paper, since measured MPI signals have no ground truth, simulation data are adopted for supervised training. Actually, the self-supervised/unsupervised learning methods do not require ground truth and therefore have the potential to apply measured data to the training of the model. Unfortunately, the methods have not yet achieved satisfactory results on MPI reconstruction. Contrastive learning is an unsupervised method, and has been applied to MPI reconstruction (Schrank and Schulz 2023). However, the trained model is only used for simple phantoms, and the reconstruction quality is inferior to traditional methods (Schrank and Schulz 2023). Hence, they were not used as the competing methods. In addition, weakly supervised learning (Zhou 2018) can be used for model training with imprecise labels, and semi-supervised learning (Van Engelen and Hoos 2020) can use unlabeled data to improve model performance. Hence, weakly supervised learning/semi-supervised learning methods also have the potential to use measured MPI signals for model training, but there is currently no relevant research in MPI reconstruction.

Several developments can be incorporated in our future work to improve the performance of our proposed method. A potential approach is to incorporate the measured MPI signals and their weak labels into the model training process by leveraging deep learning techniques such as weakly supervised learning. Furthermore, we could also use a combination of MPI reconstruction and super-resolution techniques, such as using the low-resolution phantom images and SM to produce simulation signals, and then applying signals and high-resolution images to train the network. This would enable us to leverage the strengths of both approaches and potentially improve the performance of our method.

6. Conclusion

We introduced a deep neural network called DERnet for end-to-end reconstruction in MPI. Its design draws inspiration from traditional reconstruction methods, and the data-driven approach used in DERnet enables it to effectively capture both signal and spatial information, thereby reducing the influence of noise. The experimental results demonstrate that our method can achieve competitive reconstruction efficiency and significant improvements in reconstruction quality compared with the state-of-the-art methods. This suggests that DERnet is a promising candidate method for improving reconstruction performance and may facilitate the biomedical application of MPI. Overall, the use of deep learning techniques in MPI reconstruction holds great potential for improving the accuracy and efficiency of this important medical imaging technique. By leveraging the power of artificial intelligence, we may be able to unlock new insights into medical imaging data and improve patient outcomes.

Acknowledgments

This work was supported by the National Natural Science Foundation of China under Grant Nos. 62027901, 82272111, 92159303, 81871514, 61901472,62201570, 82230067 and Beijing Natural Science Foundation under Grant Nos. 7212207, 4332058.

The inhouse and simulated data cannot be made publicly available upon publication because the cost of preparing, depositing and hosting the data would be prohibitive within the terms of this research project. The data that support the findings of this study are available upon reasonable request from the authors.

Data availability statement

The data cannot be made publicly available upon publication because the cost of preparing, depositing and hosting the data would be prohibitive within the terms of this research project. The data that support the findings of this study are available upon reasonable request from the authors.

Ethical statement

Our work does not involve human participants or animal experimentation.

ORCID iDs

Xiaopeng Ma https://orcid.org/0000-0003-4407-7045
Jie Tian https://orcid.org/0000-0003-0498-0432

References

Askin *et al* 2022 PP-MPI: a deep plug-and-play prior for magnetic particle imaging reconstruction *MLMIR, Singapore* 13587, 105–14
Baksalary O M and Trenkler G 2021 The Moore–Penrose inverse: a hundred years on a frontline of physics research *Eur. Phys. J. H* **46** 1–109
Bulte J W 2019 Superparamagnetic iron oxides as MPI tracers: a primer and review of early applications *Adv. Drug Deliv. Rev.* **138** 293–301
Bauer L M *et al* 2015 Magnetic particle imaging tracers: state-of-the-art and future directions *J. Phys. Chem. Lett.* **6** 2509–17
Chae G 2017 Neural network image reconstruction for magnetic particle imaging *ETRI J.* **39** 841–50
Coene A *et al* 2013 Quantitative estimation of magnetic nanoparticle distributions in one dimension using low-frequency continuous wave electron paramagnetic resonance *J. Phys. D: Appl. Phys.* **46** 245002
Dittmer S *et al* 2020 A deep prior approach to magnetic particle imaging *MLMIR, Lima, Peru* 12450, pp 113–22
Du Y *et al* 2019 Optimization and design of magnetic ferrite nanoparticles with uniform tumor distribution for highly sensitive MRI/MPI performance and improved magnetic hyperthermia therapy *Nano Lett.* **19** 3618–26
Gleich B *et al* 2005 Tomographic imaging using the nonlinear response of magnetic particles *Nature* **435** 1214–7
Güngör A *et al* 2023 DEQ-MPI: a deep equilibrium reconstruction with learned consistency for magnetic particle imaging *IEEE Trans. Med. Imaging* (https://doi.org/10.1109/TMI.2023.3300704)
Ilbey S *et al* 2017 Comparison of system-matrix-based and projection-based reconstructions for field free line magnetic particle imaging *Int. J. Mag. Part. Imag.* **3**
Kluth T 2018 Mathematical models for magnetic particle imaging *Inverse Probl.* **34** 083001
Kluth T, Jin B and Li G 2018 On the degree of ill-posedness of multi-dimensional magnetic particle imaging *Inverse Probl.* **34** 095006
Kluth T, Szwargulski P and Knopp T 2019 Towards accurate modeling of the multidimensional magnetic particle imaging physics *New J. Phys.* **21** 103032
Knopp T *et al* 2010 Weighted iterative reconstruction for magnetic particle imaging *Phys. Med. Biol.* **55** 1577–89
Knopp T, Gdaniec N and Möddel M 2017 Magnetic particle imaging: from proof of principle to preclinical applications *Phys. Med. Biol.* **62** R124–78
Knopp T *et al* 2020 OpenMPIData: an initiative for freely accessible magnetic particle imaging data *Data Brief* **28** 104971
Knopp T *et al* 2021 Efficient joint estimation of tracer distribution and background signals in magnetic particle imaging using a dictionary approach *IEEE Trans. Med. Imaging* **40** 3568–79
Knopp T and Grosser M 2022 Warmstart approach for accelerating deep image prior reconstruction in dynamic tomography *PMLR, Zurich, Switzerland* 172, pp 713–25
LeCun Y *et al* 1998 Gradient-based learning applied to document recognition *Proc. IEEE Inst. Electr. Electron. Eng.* **86** 2278–324
Li W *et al* 2022 Advances in magnetic particle imaging and perspectives on liver imaging *iLIVER* **1** 237–44
Li Y *et al* 2023 Modified jiles–atherton model for dynamic magnetization in x-space magnetic particle imaging *IEEE Trans. Biomed. Eng.* **70** 2035–45
Lieb F and Knopp T 2021 A wavelet-based sparse row-action method for image reconstruction in magnetic particle imaging *Med. Phys.* **48** 3893–903
Mason E E *et al* 2022 Side lobe informed center extraction (SLICE): a projection-space forward model reconstruction for a 2D imaging system *Int. J. Magn. Part. Imaging IJMPI* **8**
Paysen H *et al* 2020 Characterization of noise and background signals in a magnetic particle imaging system *Phys. Med. Biol.* **65** 235031
Quan T M, Nguyen-Duc T and Jeong W K 2018 Compressed sensing MRI reconstruction using a generative adversarial network with a cyclic loss *IEEE Trans. Med. Imaging* **37** 1488–97

Ronneberger P F and Brox T 2015 U-net: convolutional networks for biomedical image segmentation *MICCAI, Munich, Germany* 9351, pp 234–41
Rivera-Rodriguez *et al* 2021 Tracking adoptive T cell immunotherapy using magnetic particle imaging *Nanotheranostics* **5** 431–44
Schrank F and Schulz V 2023 Multi-purpose deep learning framework for MPI based on contrastive learning *Int. J. Mag. Part. Imaging* **9**
Shi G *et al* 2023 Progressive pretraining network for 3D system matrix calibration in magnetic particle imaging *IEEE Trans. Med. Imaging* **42** 3639–50
Song G *et al* 2018 Janus iron oxides@ semiconducting polymer nanoparticle tracer for cell tracking by magnetic particle imaging *Nano Lett.* **18** 182–9
Storath M *et al* 2017 Edge preserving and noise reducing reconstruction for magnetic particle imaging *IEEE Trans. Med. Imaging* **36** 74–85
Szwargulski P *et al* 2020 Monitoring intracranial cerebral hemorrhage using multicontrast real-time magnetic particle imaging *ACS Nano* **14** 13913–23
Van der Walt S *et al* 2014 Scikit-Image: image processing in Python *PeerJ* **2** e453
Van Engelen J E and Hoos H H 2020 A survey on semi-supervised learning *Mach. Learn.* **109** 373–440
von Gladiss A *et al* 2022 Reconstruction of 1D images with a neural network for magnetic particle imaging *BV Med., Heidelberg, Germany* pp 247–52
Wang S *et al* 2018 Speckle noise removal in ultrasound images by first-and second-order total variation *Numer. Algorithms* **78** 513–33
Wang Q *et al* 2020 Artificially engineered cubic iron oxide nanoparticle as a high-performance magnetic particle imaging tracer for stem cell tracking *ACS Nano* **14** 2053–62
Wang G *et al* 2022 Sensitive and specific detection of breast cancer lymph node metastasis through dual-modality magnetic particle imaging and fluorescence molecular imaging: a preclinical evaluation *Eur. J. Nucl. Med. Mol. Imaging* **49** 2723–34
Woo S *et al* 2018 Cbam: convolutional block attention module *ECCV* 11211 *(Munich, Germany)* 3–19
Yang Y *et al* 2018 ADMM-CSNet: a deep learning approach for image compressive sensing *TPAMI* 42, 521–38
Yin L *et al* 2022 Recent developments of the reconstruction in magnetic particle imaging *Vis. Comput. Ind. Biomed. Art* **5** 24
Yu E Y *et al* 2017 Magnetic particle imaging: a novel *in vivo* imaging platform for cancer detection *Nano Lett.* **17** 1648–54
Zhou X Y *et al* 2018 Magnetic particle imaging for radiation-free, sensitive and high-contrast vascular imaging and cell tracking *Curr. Opin. Chem. Biol.* **45** 131–8
Zhou Z H 2018 A brief introduction to weakly supervised learning *Natl. Sci. Rev.* **5** 44–53